



Discrete Element Modeling of Delamination in Laboratory Scale Laminated Rock

Qingwen Shi¹ · Brijes Mishra¹

Received: 25 June 2020 / Accepted: 3 September 2020 / Published online: 14 September 2020
© Society for Mining, Metallurgy & Exploration Inc. 2020

Abstract

Laminated rock can delaminate and fail under certain stress states. Delamination-caused roof fall and cutter roof failure is a common failure mechanism in roadways in Pittsburgh coal seam due to the existence of laminated shale roof. Two-dimensional numerical models were developed at laboratory scale based on the bonded particle method in order to simulate the delamination with particle flow code. In these models, an assembly of bonded particles and parallel weak planes represents the laminated rock. This model calibrated the micro-parameters of the bonded particle material and weak planes with laboratory data. The mechanism of fracturing and delamination in a laminated specimen was investigated using unconfined and confined compression test and unsupported roof compression test. The numerical results show that, under a constant horizontal stress, delamination occurs when the stress is much lower than its compressive strength. The confined compressive test indicates that delamination is restrained by applying confining stress since delamination-caused failure does not occur during any stage of the confined compressive test. Unsupported roof compression tests showed propagation of cutter roof failure with initiation of cracks and delamination at the intersections of the roof and ribs. An outer failed zone and inner failed zone form separately. The separated zones connect and form an opening in the roof. The presented numerical results provide additional insight into process of delamination.

Keywords Discrete element modeling · Laminated rock · Delamination mechanism · Cutter roof failure

1 Introduction

Pittsburgh coal seam has many longwall mines that experience frequent roof falls. The seam is overlaid with laminated shale rocks. Stack rocks are also common in coal measures strata in south West Virginia. These rocks are not structurally or geologically different from each other as they belong to the same rock type. Field observations show loss of cohesion between the laminated and stack layers. Observations from previous research have shown delamination and cutter roof failure in the roof rock [1]. The current understanding of the structural failure in these rock types is poor. Therefore, a detailed research effort is necessary in order to understand the mode of failure of laminated rocks.

There is a significant amount of literature focused on bedded and layered rock. However, there is a difference between

lamination and beds in the rock. Lamination refers to parallel layering within a bed. By definition, the bed is thicker than 1 cm, and a lamina is thinner than 1 cm [2]. Previous researches have rarely mentioned the difference between bedding and lamination. For example, Esterhuizen [3] modeled the failure of the roof with 10 cm and 30 cm beddings; additionally, Garg [4] modeled the roof as a combination of isotropic rock (matrix material within the laminates) and discontinuities. Einstein and Hirschfeld [5] tested gypsum plaster models with single joint using triaxial tests. Although the research effort on lamination is lacking, there is a significant amount of research reported on non-persistent joint rock. Due to the difficulty in reproducing the mechanical properties of the plane of weakness, i.e., the cohesion, stiffness, and frictional coefficient, some researchers used the non-persistent joint model (Fig. 1), both experimentally and numerically [6]. Arora and Mishra [7] determined the mechanical behavior of shale using a biaxial testing device; however, they did not investigate the delamination process.

The parameters of a joint or weak plane model such as shear and normal stiffness cohesion significantly affect the behavior of the complete rock both in intact and rock mass condition. Researchers have performed significant work on

✉ Qingwen Shi
wvuqingwenshi@gmail.com

¹ Department of Mining Engineering, West Virginia University, Morgantown, WV 26505, USA

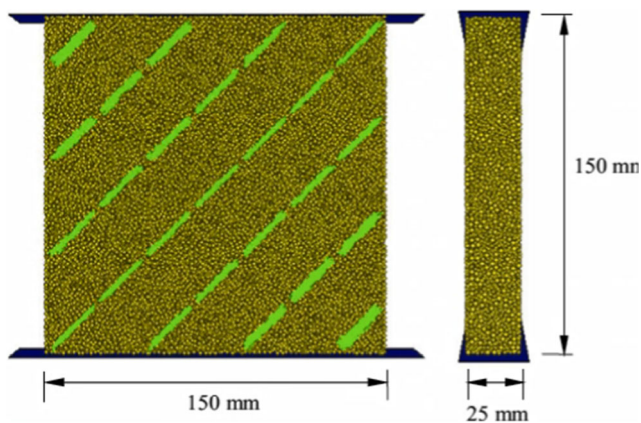


Fig. 1 Non-persistent model [6]

simulating rock with joints or weak plane, providing various insights on how to assign parameters to the model. Loong [8] simulated the effect of a single joint angle under uniaxial and triaxial compression with 3DEC. Their results were in good agreement with the theoretical results (Fig. 2) [9], validating the feasibility of using DEM to investigate the jointed rock mass. However, the research effort did not discuss the calibration of joint parameters. Oh et al. [10] studied the dilation angle of a saw-toothed rock joint under direct shear and found the dilation directly depend on the normal stress. Chiu [11] used Yang's laboratory data [12] to simulate a modified smooth-joint model and showed that the modified smooth-joint model simulated the mixed and sliding modes of artificial rock mass. Lambert and Coll [13] assessed the shear strength of a discontinuity using numerical models that included joints with asperities combined a real 3D surface morphology and the smooth-joint contact model.

The research approach mentioned in earlier sections used joints to simulate bedding planes that cannot be applied to

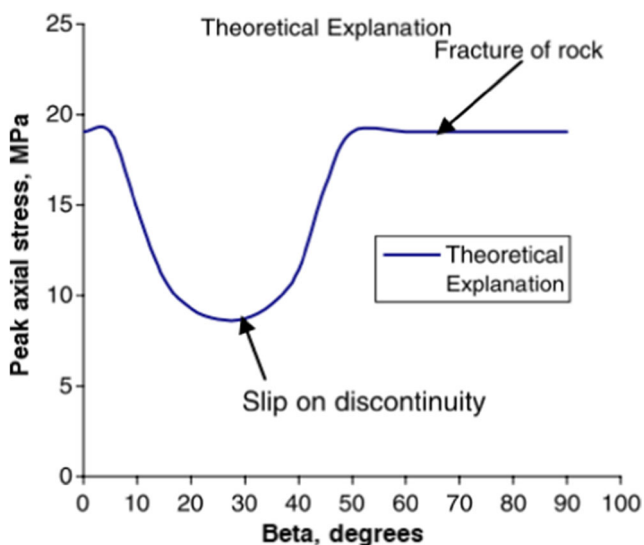


Fig. 2 Theoretical results for a specimen with inclined joint [9]

laminated shale. The joint models have predefined stiffness that restricts delamination and therefore cannot explain the intrinsic process of delamination of a laminated rock under various boundary conditions.

When comparing the modeling methods and the joint models, PFC is uniquely able to simulate the crack development and the smooth-jointed model. The inherent constitutive models in PFC are capable of modeling both the frictional and cohesive planes. The present research used particle flow code (PFC) to simulate the laminated rock. This research also implemented the smooth-joint model to simulate the weak plane between laminas and parallel bond model to simulate the matrix. The calibrated models investigated the delamination process under different boundary conditions at a laboratory scale. The research will provide further understanding in the process of delamination.

2 Methodology

In PFC, the jointed rock mass is developed using three methods [14]: (1) bond-eliminated model, (2) band-eliminated model, and (3) smooth-joint model. Smooth-joint model is characterized by eliminating the roughness resulting from the particle arrangement. The bond-eliminated model involves applying a plane through the specimen and eliminating the bonds through the plane to separate the whole model into blocks. This method is easy to use; however, the joint face may have inestimable roughness because of the interlock between particles on the joint face. Instead of inserting a plane without thickness, the band-eliminated model eliminates the bond within a broad band through the specimens that reduces the particle-interlocking problem. However, there is considerable difficulty in controlling the normal displacement on the joint face. In the smooth-joint model, the particle pair is intersected by a smooth joint to overlap and pass through each other instead of moving around one another [15]. As such, this model improves the influence of these two techniques and eliminates the roughness resulting from the particle arrangement.

In the present study, the laminated rock is composed of laminas and planes of weakness. This research used the parallel bond model to model the laminas and the smooth-joint model to represent the plane of weakness. The micro-parameters are calibrated based on the laboratory testing data from Yang's experiments [12]. Yang fabricated brittle rock with a mixture of plaster, sand, and water in the proportions of 1:0.25:0.92. This study also created an artificial frictional weak plane using a controllable double-blade guillotine with 60°-wedge blades. Direct shear test performed on this artificial weak plane provided mechanical parameters for the plane.

The parameters of lamina were obtained by calibrating the parallel bond model with the laboratory data for intact rock.

To obtain the parameters of the weak plane, the smooth-joint model was calibrated with the laboratory data from direct shear tests by simulating a direct shear model in the PFC. Then, the lamina and weak plane parameters are combined together to create the laminated rock mass model. The effect of joint angle on mechanical behavior of a jointed rock was investigated through simulated triaxial compression tests. The results were then validated by comparing with the rock mass magnitude. The procedure to simulate the laminated rock model is shown in the flow chart in Fig. 3.

3 Calibration

3.1 Calibration of Laminas

Based on the laboratory tests, the uniaxial compressive strength is 7.63 MPa, the direct tensile strength of the rock is 1.05 MPa, Young's modulus is 4.55 GPa, and the internal friction angle is tested as 31° .

Following the calibrating procedures recommended by Itasca [16], the micro-parameters of matrix, including Young's modulus, direct tensile strength, and uniaxial compressive strength, are calibrated as shown in Fig. 4 and Fig. 5.

Finally, the confined compression strength tests with servo-control mechanism were simulated using confining pressures of 2.5, 5.0, and 7.5 MPa. Table 1 shows the test results of both the direct tensile and unconfined compressive test. Figure 6 shows the Mohr envelope of the specimen matrix.

Table 2 shows all the calibrated results as compared with laboratory results. The macro-parameters of the bonded

particle model are in good agreement with the tested specimens in the laboratory. Table 3 lists all calibrated micro-parameters.

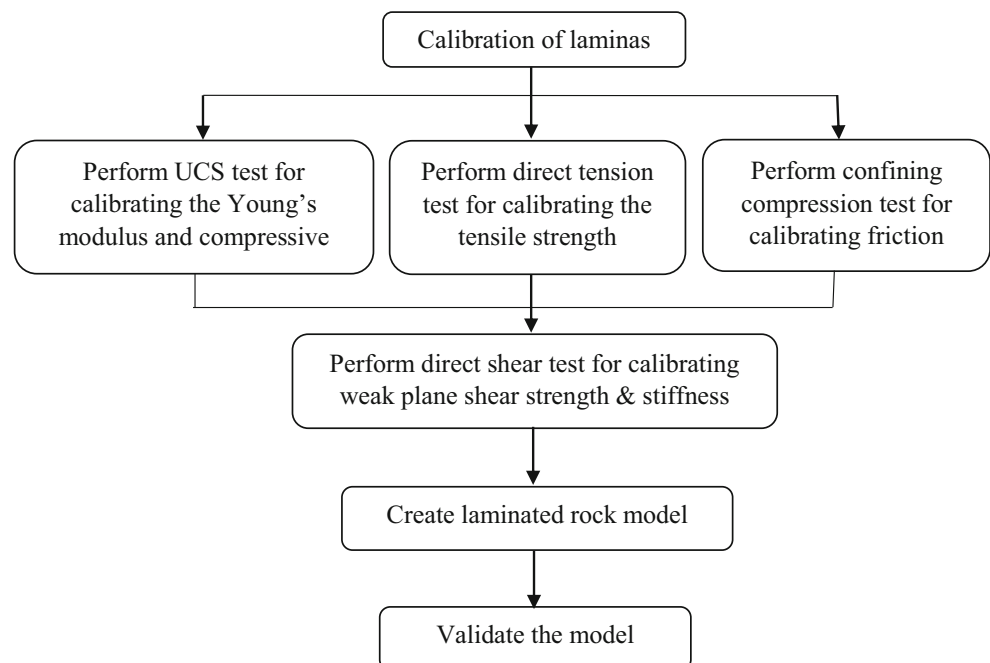
3.2 Calibration of the Weak Planes

As mentioned in earlier sections, mechanical parameters play a dominant role in determining the behavior of the entire specimen. It is therefore imperative to calibrate the weak planes in the numerical model. The present research used direct shear test to obtain the mechanical parameters and calibrate the weak planes in the models. The data was used from the direct shear test on a frictional weak plane with zero cohesion value of the weak plane. Figure 7 shows the direct shear conducted under a normal stress of 0.63 MPa in lab [12]. The shear stiffness of the weak plane is 0.48 GPa, and the shear strength is 0.96 MPa.

We developed a direct shear model composed of parallel bond particle as matrix and smooth-joint fracture as a frictional weak plane in PFC2D as shown in Fig. 8a. The red line represents location of the smooth-joint plane. The servo-control mechanism applied normal stress to the top of the specimen. The model simulated the shear process by moving the upper platen horizontally over a fixed lower platen.

In the numerical model, the upper platen displacement and the shear stress along the weak plane were monitored. The shear stiffness and shear strength were calibrated through a trial and error approach. The calibrated results with a shear stiffness of 0.45 MPa and shear strength of 0.98 MPa show good correlation with the laboratory data as observed in Fig. 9.

Fig. 3 Procedure to simulate the laminated rock model



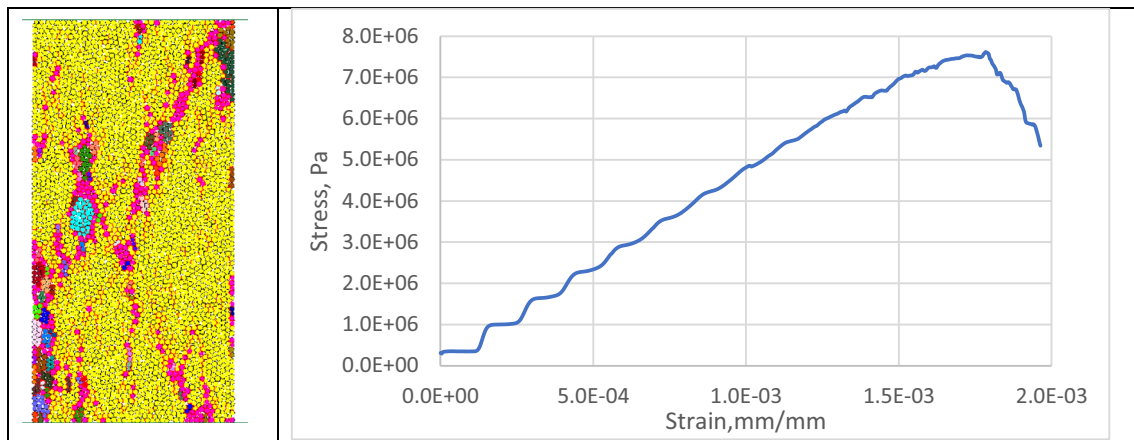


Fig. 4 Calibration of Young's modulus and uniaxial compressive strength

This showed that the simulated weak plane matched the actual behavior of weak plane in an intact rock. Table 4 lists the parameters used for the smooth-joint model.

3.3 Validation of Combined Micro-Parameters

We conducted a series of confined compressive tests on an inclined single joint specimen to validate the combination of parallel-bond model and smooth-joint model as shown in Fig. 10. The confined stress was set at 1.0 MPa, and the results were compared with theoretical conclusions [9].

Figure 11 plots the compressive strength of the specimens with different orientations. The curve is in good agreement with theoretical results validating the feasibility of the combination of parameters for parallel bond model and smooth-joint model as shown in Fig. 2. Figure 12 shows the stress-strain curves for these specimens. In this figure, it is observed that the specimens with 30–70° orientations have low overall Young's modulus and low strength. This is due to the sliding along the plane of weakness.

4 Delamination Simulation

The cutter roof failure or kink failure in coal mines occurs in laminated rock with significant delamination. Therefore, it is imperative to understand the vital mechanism of this particular roof failure. Hill [1] and Molinda [17] discussed the causes and methods for control of roof failure with no unique solution for controlling or avoiding cutter roof failure. Esterhuizen [3] modeled the failure of the roof with 10 cm and 30 cm beddings and found that cutter roof failure has different characteristics varying with mines. Becker [18] investigated the cutter roof failure in Carroll Hollow Mine, Ohio, with numerical models and found that the localized perturbed state of stress in combination with geometric factors caused cutter roof failure. Gao [19] and Murphy [20] discussed the failure mechanics associated with the weak characteristics of bedding rocks and concluded that the horizontal stress is the main contributing factor in the deterioration of a weak roof and contributor to cutter roof failure. Ghabraie et al. [21] confirmed the reinforcing effect of the truss bolt system in an underground excavation in layered rock using non-linear finite element analysis.

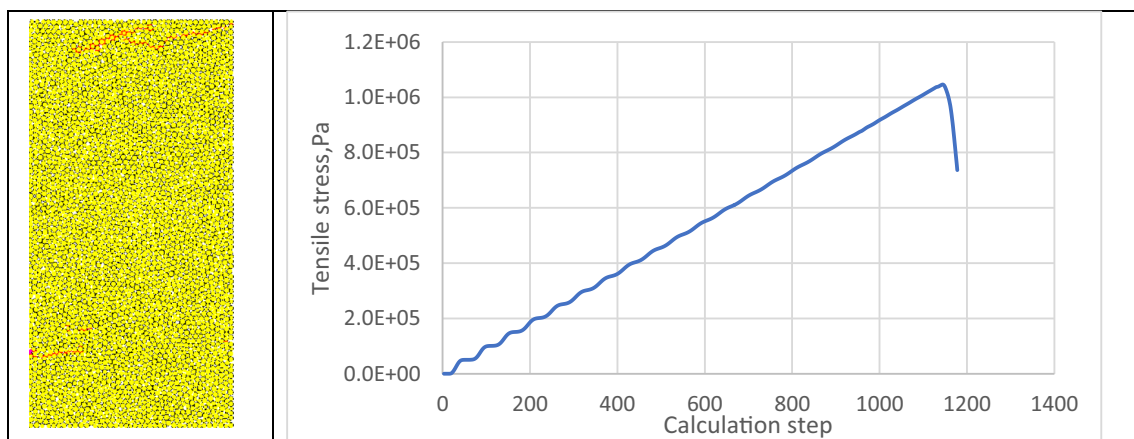


Fig. 5 Calibration of direct tensile strength

Table 1 Compressive test results under different confining stress

Direct tensile strength, MPa		Unconfined stress		Confining stress = 2.5 MPa		Confining stress = 5.0 MPa		Confining stress = 5.0 MPa	
σ_3	σ_1	σ_3	σ_1	σ_3	σ_1	σ_3	σ_1	σ_3	σ_1
-1.05	0	0	7.6	2.5	17.5	5.0	25.1	7.5	33.5

σ_3 the applied minimum principle stress, σ_1 the applied maximum principle stress

Xue [22] numerically studied the size effect of laminated rock with FLAC3D. Previous studies provide good understanding of the characteristics and contributing factors of cutter roof failure. Rare attention, however, has been paid to the process of cutter roof failure.

With the validated micro-parameters obtained in earlier sections for both the lamina and the weak plane, laboratory scale laminated rock specimens were built in PFC2D with dimensions of 150 mm in length and 80 mm in height. The specimens were simulated with uniaxial and triaxial boundary conditions. This was then followed by simulation of an unsupported roof under compression test to observe the failure process of laminated specimen under different stress conditions. Figure 13 shows the schematic diagrams of these models. Focusing on development of delamination, the following sections discuss the tests on these models in detail.

The simulation consists of the following different conditions to which the model is tested:

- (1) Uniaxial compressive test subjected to incremental horizontal stress.
- (2) Uniaxial compressive test subjected to various constant horizontal stresses.
- (3) Confined compressive test subjected to incremental horizontal stress.
- (4) Compressive test on unsupported roof model subjected to incremental horizontal stress.

Steps (1) to (3) focused on the unconfined and confined effect of the delamination under various horizontal stresses. Step (4) simulates the stress state, which is commonly

observed in underground-unsupported entries. Step (1) also investigated the effect of lamina thickness on delamination.

4.1 Uniaxial Compressive Test Subjected to Incremental Horizontal Stress

Figure 14 shows the smooth-jointed laminated model. The red lines represent the parallel joints and the yellow particles represent the laminas. The uniaxial stress in the model represents the horizontal stress. The model applied this stress by moving boundaries at a constant velocity, which can cause an incremental horizontal stress. The moving velocity of the platens was 0.01 m/s. This study recorded observations of the model behavior throughout the test. Figure 15 shows the strain-stress curves for all the models, including the intact rock and laminated specimens with various lamina thicknesses.

This study then conducted an analysis on laminated rock specimen with a lamina thickness of 4, 5, 6, 7, and 8 mm.

Figure 15 shows that the laminated rock strength increased with the thickness of lamina. Therefore, thick lamination will sustain high horizontal stress. Similarly, the stiffness of the specimen will also increase with an increase in the lamina thickness. In addition, the peak stress occurs at different strain magnitudes for these curves as shown in Fig. 15. For example, the 8-mm lamina specimen reaches its peak stress when the strain is 0.0011, while the 4-mm lamina specimen reaches its peak at the strain of 0.0008, indicating that the thinner lamina will bring about smaller strain value where peak strength is reached. From the model results, it is concluded that the thickness of the lamina in laminated rock significantly affects the macro-behavior, e.g., along-lamina stiffness, along-lamina strength, and the maximum strain it can sustain before failure.

Figure 16 shows the sequence of the delamination process captured from the numerical simulation. As shown by the legend, the black lines represent the compressive force chain in the specimen, while the red lines represent the tensile force chain, which is not noticeable during the test. The boldness of these lines represents the relative magnitude of the force. The red cracks represent the fractures, which indicate unbonded particles. The colored particles represent the fragments in the specimen and the same color indicates a piece of fragments that comprise of a clump of bonded particles. Different colors of fragments indicate that the fragments are separated due to the development of the fractures. The colored arrows represent

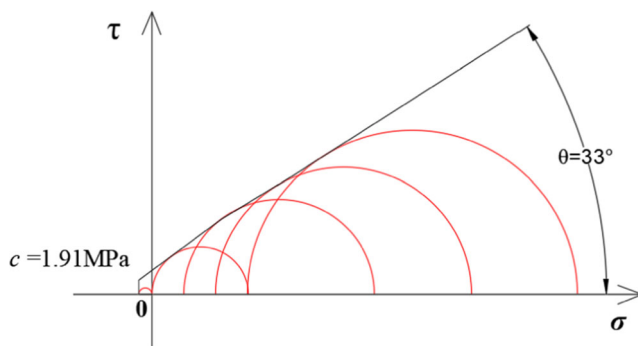


Fig. 6 The Mohr envelope of the parallel bonded model

Table 2 Comparison with the numerical and laboratory results

	Unconfined compressive strength, MPa	Direct tensile strength, MPa	Young's modulus, GPa	Angle of friction, degrees
Laboratory results	7.63	1.05	4.55	31
Numerical results	7.62	1.05	4.50	33

the particle moving velocity under the horizontal stress and the size of the arrows represents the magnitude of the velocity.

In Fig. 16a, at the initiation of the test, the force chain inside the specimen includes various separate force chains that exist inside the laminas. This is because the laminas are mechanically disconnected with each other, as there is no cohesion between the laminas. The force chains do not connect at all, indicating that there is no vertical force between the laminas. As such, it is concluded that the laminas are acting independently under horizontal stress in an unconfined condition.

At 41% of its uniaxial compressive strength, the specimen develops fractures at its left end. In addition, the initiation location is inside the specimen instead of on the edge of the specimen. Figure 16 c shows the localization of fractures at the initiation point and progressively change in the force chain shape with every increment in the compressive stress indicating the transfer of force. Subsequently, cracks occur at different places on the edge of the specimen (Fig. 16d, e).

The delamination does not occur until the compressive stress exceeds 96% of its compressive strength (Fig. 16f). In Fig. 16f, failure occurs in the fifth lamina from the top. This lamina is represented by three colors: left section in gray, middle section in green, and right section in blue, demonstrating lamina failure. The particle velocity further validates this lamina's failure. As seen in the velocity distribution picture in Fig. 16f, the left gray section moves towards right while the right blue section moved to the lower left. In addition, the upper lamina moved upward vertically and the lower lamina moved downward vertically. This showed the laminas moved

apart, indicating the occurrence of delamination. At the same time, the fifth lamina slides relative to its upper and lower laminas, which is another indicator of the delamination. In Fig. 16f, the entire left section of the fifth lamina moved to a new position. In addition, particles also moved in opposite directions in various localized sections indicating the breakage of lamina. Surprisingly, the specimen failure did not occur when the laminas moved in the outward direction.

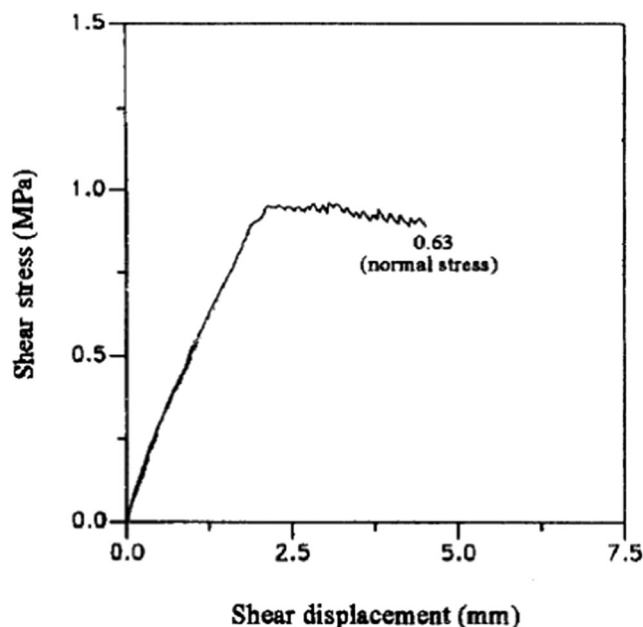
When the compressive stress reaches exactly the compressive strength of the specimen, force chain boldness of the third and fifth laminas from the top decreased to zero, which indicated loss in strength, as shown in Fig. 16g. However, at the same time, the lamina between them (third lamina from the top) still maintained the stress shown by the force chain's boldness. This indicated that the failure of lamina is not continuous and therefore, the failed lamina and non-failed lamina may occur alternatively at a specific point of time.

After the compressive strength test, the laminated specimen did not completely disintegrate due to the residual strength. When it reached 86% of the compressive strength in the post-peak stage, the upper five laminas fade, indicating a loss in strength, as shown in Fig. 16h. Similarly, this behavior occurs in the bottom outer lamina. Since the applied stress continues to work, more laminas adjacent to failed ones are losing their strength, which results in expanding delamination scope and

Table 3 Micro-parameters utilized for the parallel bond particle model

Parameters	Values
Particle radius, mm	0.5–0.75
Material density, kg/m ³	2500
Bond gap	0.5e–4
emod, GPa	2.219
<i>k</i> ratio	1.0
<i>pb_ten</i> , MPa	1.538
<i>pb_coh</i> , MPa	4.5
<i>pb_fa</i> , degrees	31
Ball-ball friction	0.4

emod parallel bond effective modulus, *k* ratio parallel bond normal-to-shear stiffness ratio, *pb_ten* parallel bond tensile strength, *pb_coh* parallel bond cohesion, *pb_fa* parallel bond friction angle

**Fig. 7** Direct shear test in lab [12]

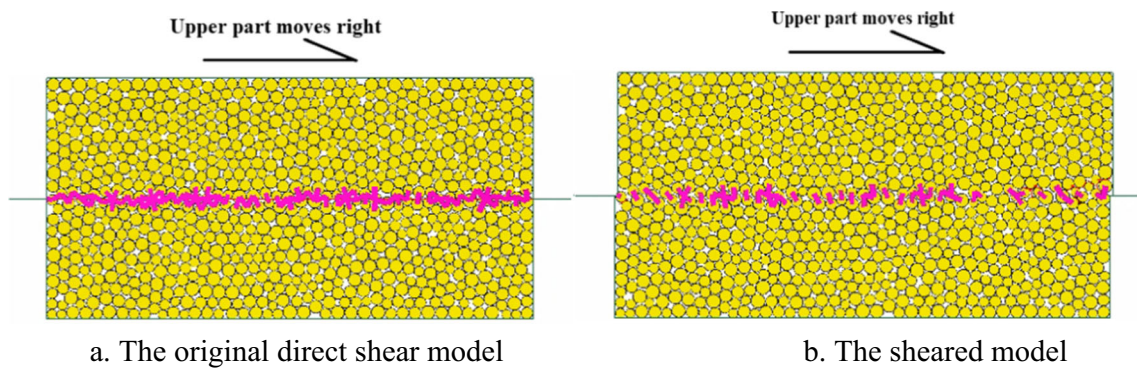


Fig. 8 The direct shear model. **a** The original direct shear model. **b** The sheared model

seriousness. Finally, the specimen dilates even after the complete disintegration of the specimen, as shown in Fig. 16 i, j, and k.

4.2 Uniaxial Compressive Test Subjected to Various Constant Horizontal Stress

In underground roadways, the horizontal stress usually remains relatively constant after excavation of the roadways. Therefore, it is important to investigate the process of delamination of the laminated specimen under constant horizontal stress. In this section, varying constant horizontal stress is applied to the 5-mm lamina specimens.

When the horizontal stress is at 41% of the compressive strength, the contact force chains maintain their original shape and magnitude. Only limited fractures occur within the specimen, as shown in Fig. 17. This indicates that the delamination will not occur under this magnitude of compressive stress.

However, when the horizontal stress increased to 42% of the compressive strength, delamination occurred in the specimen after 30,000 time steps as the adjacent laminae inside moved in the opposite directions as shown in Fig. 18a. Therefore, the complete specimen is delaminated with its upper half moved upward while the lower half moved downward. With every increment in the calculation step, the delamination becomes more pronounced. As shown in Fig. 18b, one

lamina separated completely from both its upper and lower half with reduction in the strength, partially due to the opposite moving direction of these two parts. However, in comparison with Fig. 16f, the delamination only initiated from one lamina, while this occurred at multiple places in Fig. 16f. With the calculation step at 1,600,000, the whole specimen loses its strength. This is similar to roof fall that occurs in mines due to loss in strength.

Therefore, the delamination may occur under a constant horizontal stress, which is much lower than its compressive strength. In addition, the laminated specimen may completely lose its strength under constant stress.

4.3 Confined Compressive Test Subjected to Incremental Horizontal Stress

The roof is reinforced with a support system such as roof bolts that provides confining pressure to the laminated roof. The present section observed both the failure process and mode under confined compressive state. In this section, the confined stress is set at 1.0 MPa through servo-control mechanism in PFC2D. In order to make a comparison with the tests under uniaxial compressive state in Section 4.1, all geometrical and mechanical parameters, including dimension, lamina thickness, lamina, and weak plane micro-parameters, are set to be the same as the model in Section 4.1. Figure 19 shows the full stress-strain curve of this test in which the confined compressive strength is 7.9 MPa. This figure shows that the monotonic portion of the stress-strain curve is nearly a straight line, which is similar to a uniaxial compression test. Instead of a sharp drop in stress after failure, residual strength is observed under the confining stress.

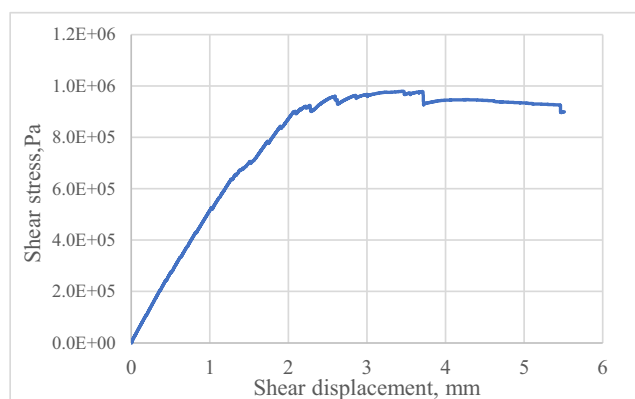


Fig. 9 Simulated direct shear test

Table 4 The calibrated micro-parameters for smooth-joint model

Parameters	sj_kn, GPa	sj_ks, GPa	sj_fric	sj_coh	sj_ten	sj_large
Values	200	9.9	2.3	0	0	1

sj_kn smooth-joint normal stiffness, *sj_ks* smooth-joint shear stiffness, *sj_fric* smooth-joint friction coefficient, *sj_coh* smooth-joint cohesion, *sj_ten* smooth-joint tensile strength, *sj_large* smooth-joint bond type

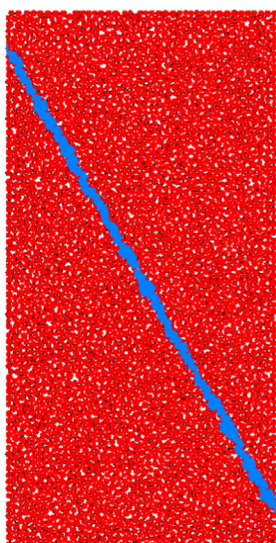


Fig. 10 Rock specimen with a 60° oriented joint

Figure 20 depicts the force chain, particle moving velocity, lamina fragment, and fracture developing process. The signs and their physical meanings are the same as described in earlier sections. The figure showed that the force chains connect to each other, in comparison with those from uniaxial test in Fig. 16a. This showed that the laminas mechanically connect with each other due to the confining pressure. Therefore, the laminated specimen acts as if complete instead of carrying the load independently as in uniaxial test.

The fractures initiate at the edge of the specimen when the stress reached 46% of the strength, as shown Fig. 20b, which is marginally higher than the uniaxial test at 41%. As the horizontal stress continued to increase, these fractures continued to develop and progressively change the shape of the force chain at the left end of the specimen in Fig. 20c, indicating the change in the force distribution.

When the horizontal strength reached 78% of the confined compressive strength, the lamina fractures inside the specimen. As shown in Fig. 20d, the particles in the same lamina

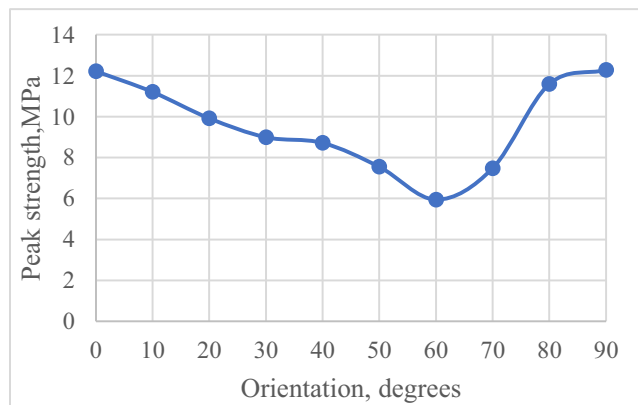


Fig. 11 Compressive strength with various inclined weak planes

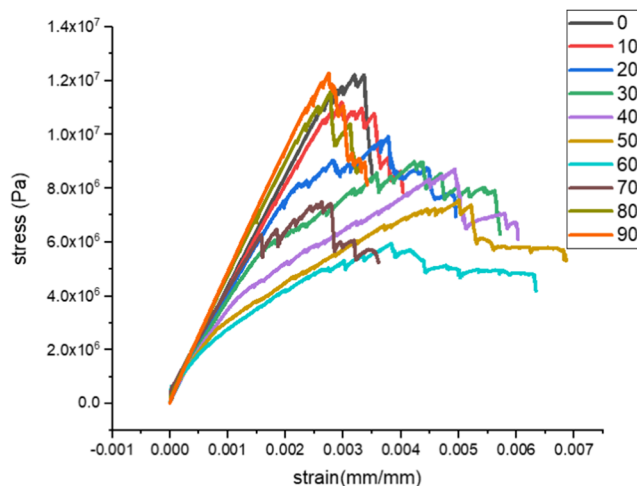


Fig. 12 Stress-strain curves for specimens with orientation of bedding planes

moved towards the opposite directions and interacted with the fragments. The same case occurs in several more laminas in the specimen when the compressive stress reached 96% of the confined compressive strength as shown in red circles in Fig. 20e. It is also observed that some small sections are separated from these laminas as highlighted by red circles that causes the shape change of their force chains. However, these laminas still do not completely fail, as their force chains are still capable of carrying load.

The lamina disintegrates into small sections when the peak value is exceeded (Fig. 20f). The test proceeds into post-peak stage in which the laminas continue to fail and disintegrate into small pieces until the specimen is completely disintegrated (Fig. 20g).

The delamination failure mode that occurred in uniaxial compressive test does not occur during any stage of the confined compressive test. Therefore, this study concluded that by applying supporting systems to the laminated roof, it is possible to restrain delamination; e.g., roof bolting or secondary support can apply confining stress to the free face of the roof.

4.4 Compressive Test on Unsupported Roof Model Subjected to Incremental Horizontal Stress

This section simulated an unsupported roof model in laboratory scale. Figure 13 c shows the schematic diagram of the model. The rigid boundaries in the lower corners are the supporters provided by ribs of roadway. Figure 21 shows the unsupported roof model established in PFC2D in order to investigate the failure propagation in such a stress state. All the micro-parameters and geometric dimensions are the same as the models in earlier sections except for the boundary conditions. The model is initiated with a hydrostatic stress state set at 1.0 MPa. The test applied horizontal stress until complete loss in the strength of the roof.

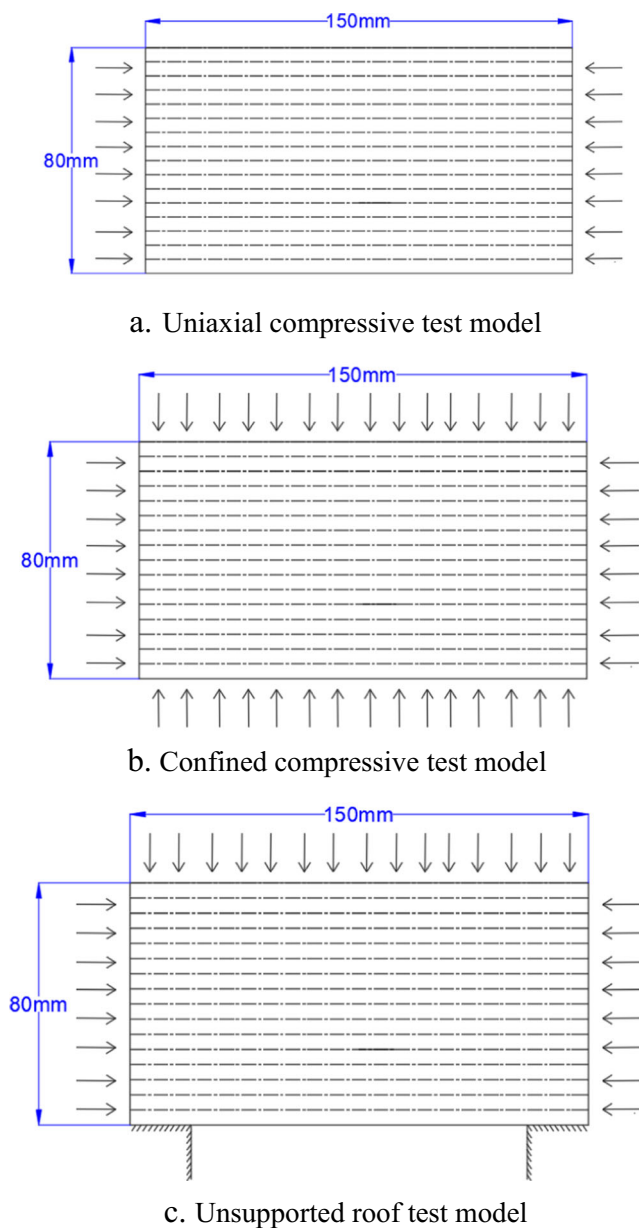


Fig. 13 Simulation sequence. a Uniaxial compressive test model. b Confined compressive test model. c Unsupported roof test model

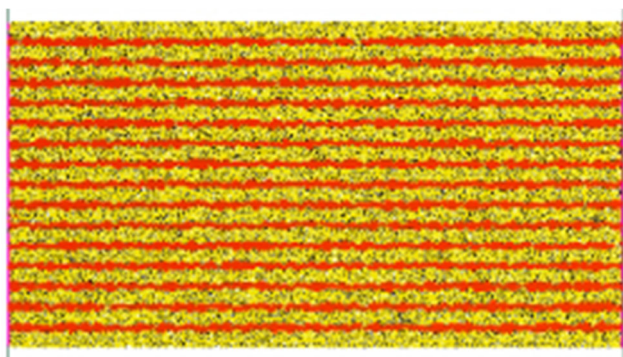


Fig. 14 Laminated rock model

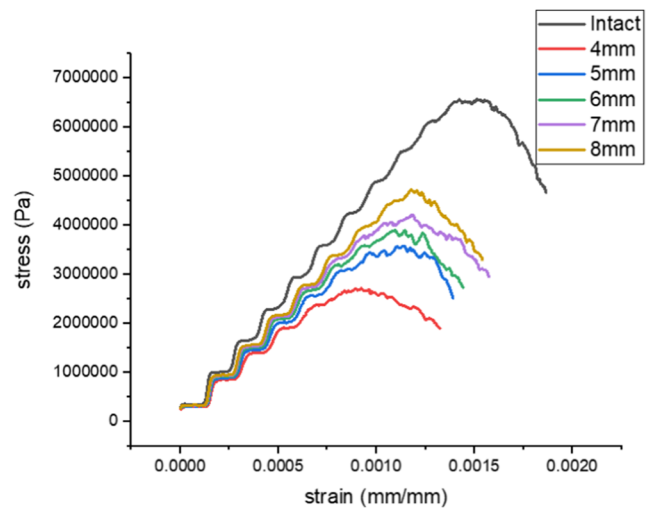


Fig. 15 Stress-strain curves for specimens with different lamina thicknesses

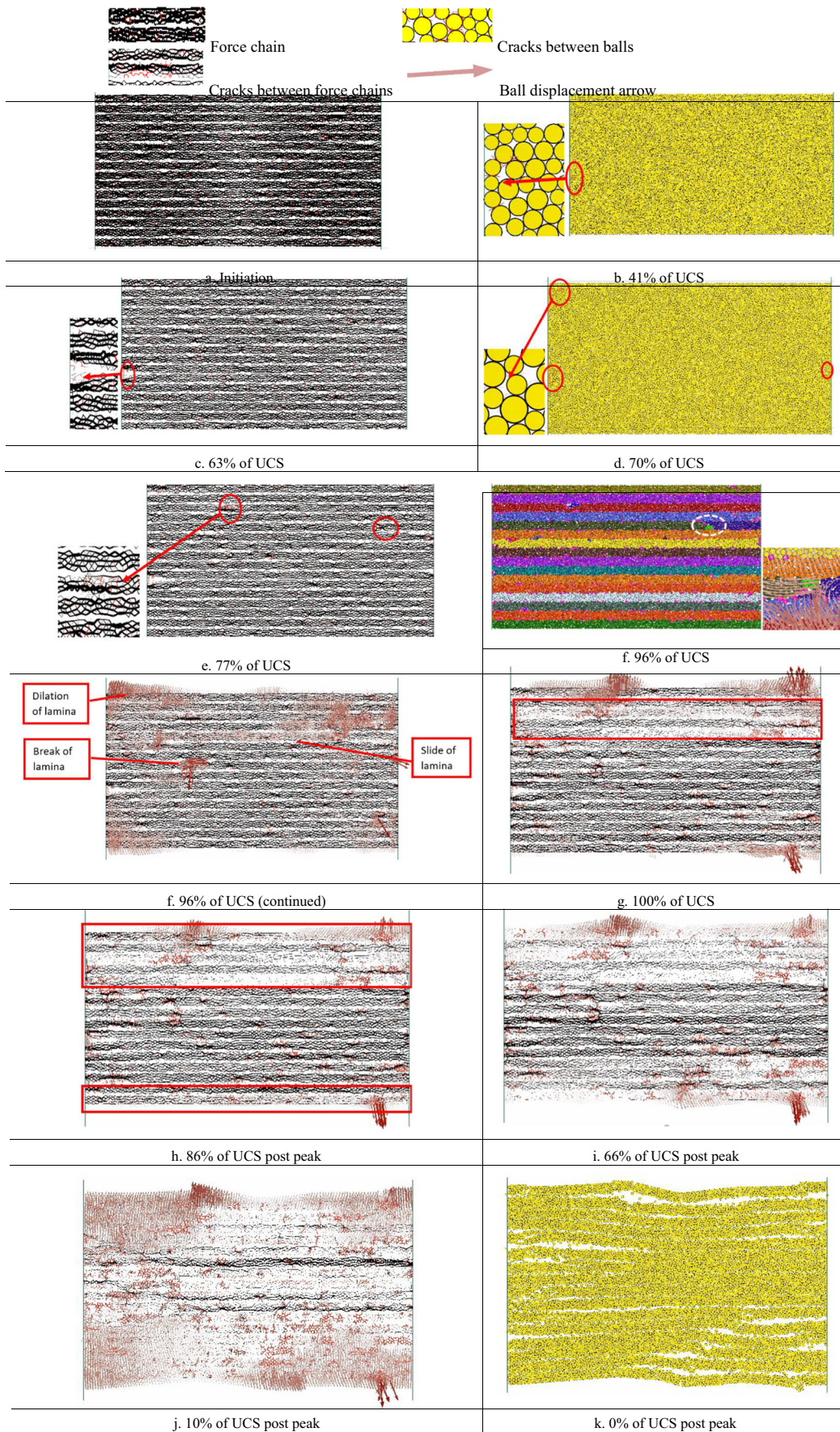
Figure 22 shows the stress-strain curve obtained after the test is completed. The strength of the unsupported roof is 3.5 MPa that matches the uniaxial compressive strength in Fig. 15 and much lower than the confined compressive strength in Fig. 19.

Figure 23 depicts the force chain, particle moving velocity, lamina fragment, and fracture developing process. The signs and their physical meanings are the same as in earlier sections.

The cracks initiate from the two bottom corners of the specimen, which represents the intersection of the roof and ribs as shown in Fig. 23. With the increase in the horizontal stress, the bottom lamina moves downward to its left side adjacent to the intersection. This causes delamination at this location as shown in Fig. 23b, which is in good agreement with field observations of cutter roof failure. Next, the right side of this bottom lamina starts to delaminate as well. Figure 23 c shows that the delamination of this lamina gradually caused its failure, as demonstrated by the faded force chain of the bottom lamina.

The next failed lamina is not the one adjacent to the bottom lamina. Instead, the inner lamina showed delamination. As shown in Fig. 23d, the particles moved in opposite directions in the fifth lamina from the bottom of the specimen when the horizontal stress reached 80% of its strength, indicating the initiation of lamina failure. Figure 23 d further verified this failure by showing its faded force chain. Immediately after the fifth lamina failed, the sixth lamina failure occurs, shown by the faded force chain in Fig. 23e. This created two separate failed zones in this specimen, i.e., the outer failed zone and inner failed zone. These zones are separated by several intact laminae between them.

The second lamina from the bottom does not fail until the horizontal stress reaches its peak value, i.e., the strength of this specimen as shown in Fig. 23f. The particles of this lamina moved horizontally at a relatively high velocity. This causes



◀ **Fig. 16** Development of the delamination. **a** Initiation. **b** 41% of UCS. **c** 63% of UCS. **d** 70% of UCS. **e** 77% of UCS. **f** 96% of UCS; 96% of UCS (continued). **g** 100% of UCS. **h** 86% of UCS post-peak. **i** 66% of UCS post-peak. **j** 10% of UCS post-peak. **k** 0% of UCS post-peak

the lamina force chain to weaken, as shown in the force chain map in Fig. 23f. Afterwards, the test moved into the post-peak stage where the intact laminas lose their strength one by one until the separate failed zones connect with each other as shown in Fig. 23g. Next, the failed zones develop upward until the whole specimen loses its strength, as shown in Fig. 23 h and i. The failed roof mass continued to fail and formed an opening as observed in the field.

5 Conclusion

This paper presents a numerical investigation of delamination process of a laboratory scale laminated specimen with frictional weak planes. This study created both laminated rock with parallel bond model and smooth-joint model in PFC2D. Calibrated models are validated by the confined compressive tests on specimens with varying plane orientation. The validated laminated model implemented the compressive tests under various boundary conditions and investigated the crack development and delamination propagation during these tests.

Uniaxial compressive tests with various lamina thicknesses show that the thickness of the lamina significantly affects the macro-parameter of the laminated specimen, including along-lamina stiffness, along-lamina strength, and the maximum strain it can sustain before failure. Increased in the thickness of the lamina caused an increase in the macro-parameters.

The delamination propagation analysis of uniaxial compressive tests showed that the delamination of an unconfined specimen begins on the inside laminas instead of outer ones. Delamination does not occur until the compressive stress matched the UCS when applying incremental stress to the specimen. However, delamination occurred under a constant horizontal stress, which was much lower than its compressive strength. The modeling results confirmed that delamination is

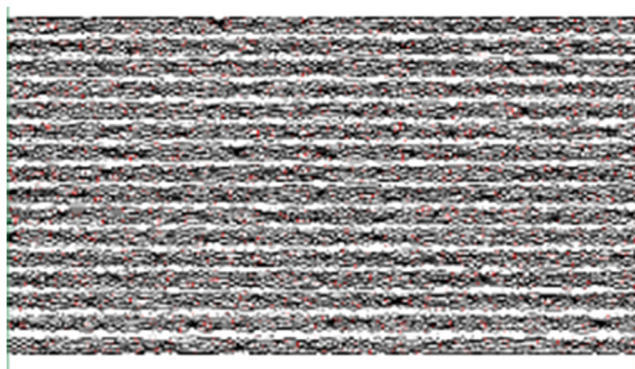


Fig. 17 Horizontal stress at 41% of compressive strength

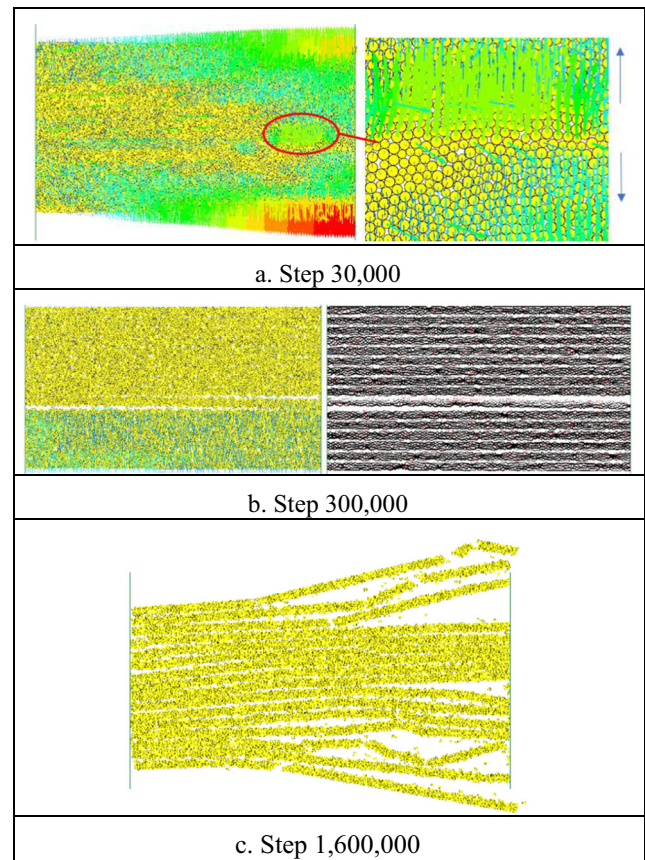


Fig. 18 Horizontal stress = 42% of compressive strength. **a** Step 30,000. **b** Step 300,000. **c** Step 1,600,000

prevented by applying confining stress. The compressive test on an unsupported roof model showed the cutter roof propagation and delamination initiated at the intersections of the roof and ribs. Before roof fall, separate failed zones in this specimen will form, i.e., outer failed zone and inner failed zone. These zones are separated by several intact laminas between them. The separate failed zones connect with each other as the intact laminas weaken and finally create a massive failure. This research showed the mechanism involved in roof delamination. The effect of interface parameters such as

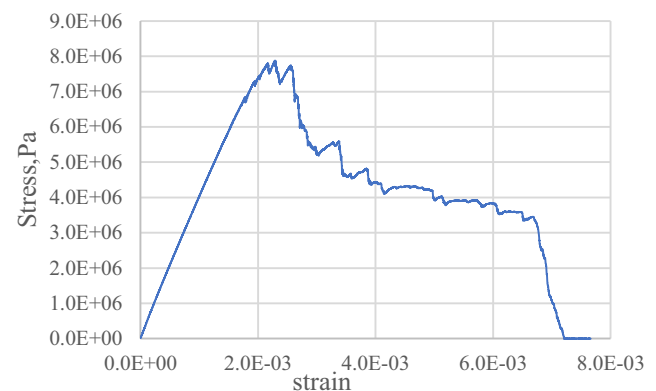


Fig. 19 Full stress-strain curve of the confined compressive test

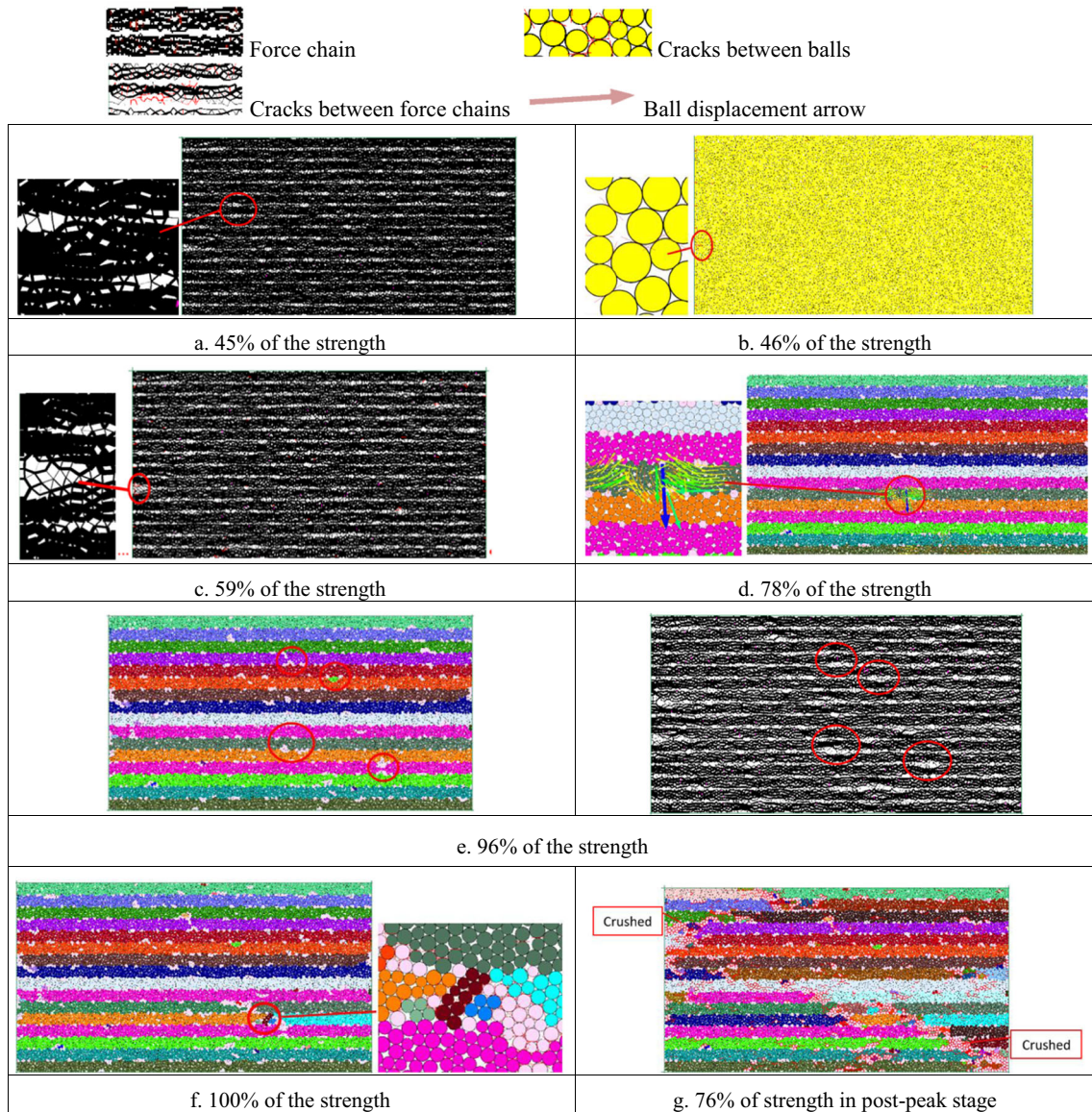


Fig. 20 Failure propagation in the confined compressive stress test. **a** 45% of the strength. **b** 46% of the strength. **c** 59% of the strength. **d** 78% of the strength. **e** 96% of the strength. **f** 100% of the strength. **g** 76% of strength in post-peak stage

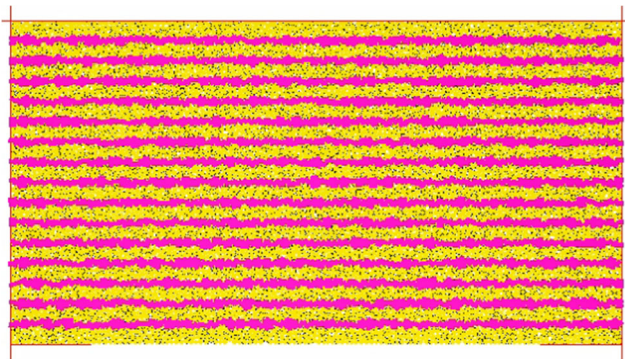


Fig. 21 Unsupported roof model

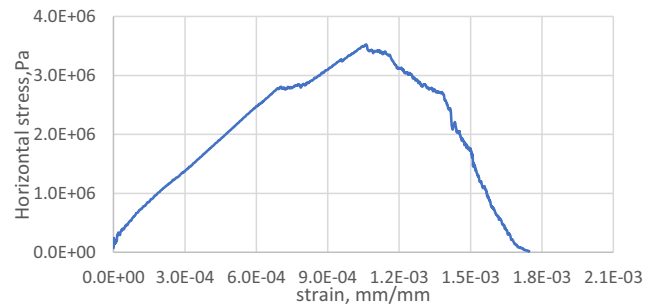


Fig. 22 Full stress-strain curve of the unsupported roof model

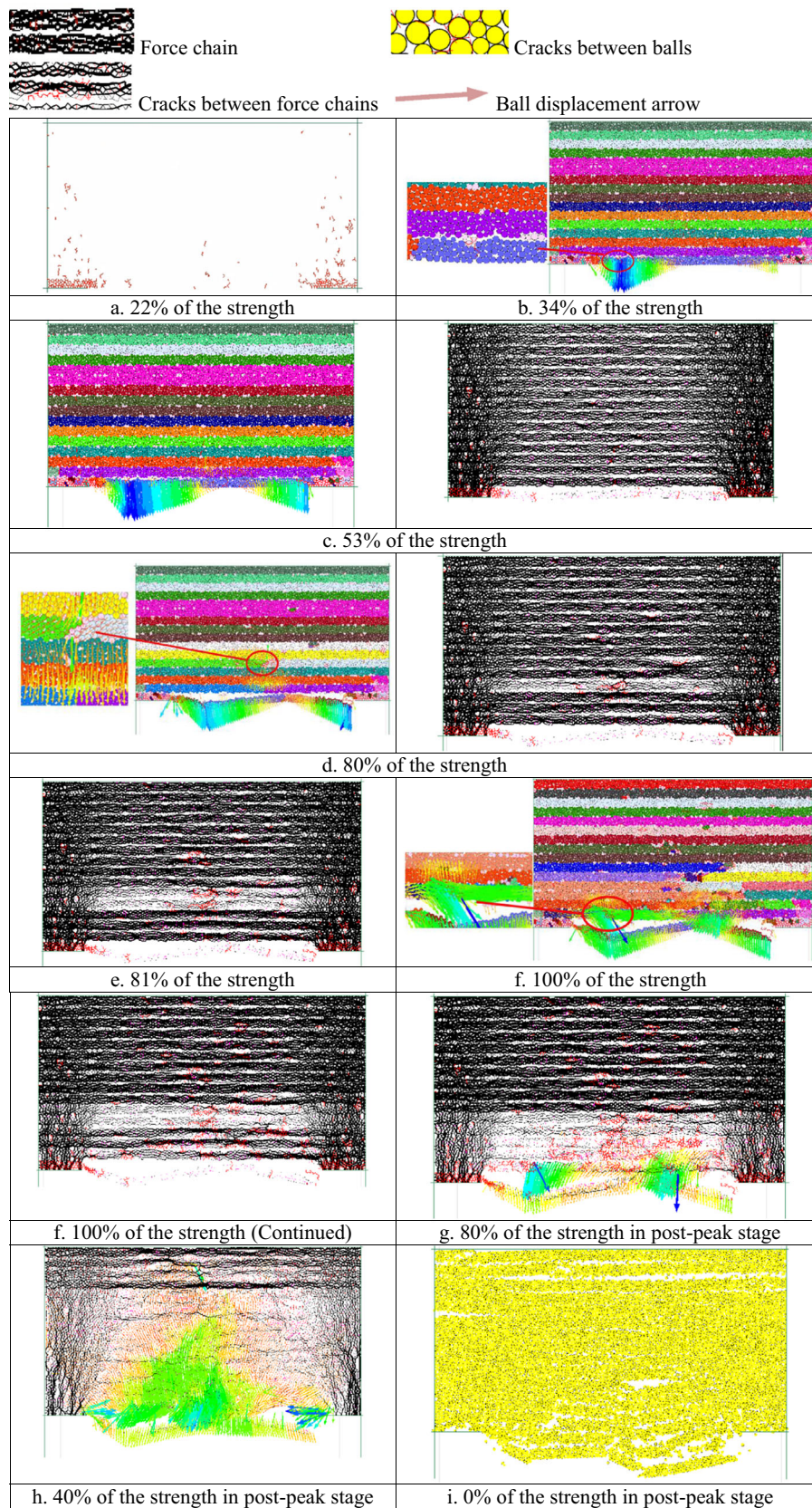


Fig. 23 Cutter roof failure propagation of the unsupported roof model. **a** 22% of the strength. **b** 34% of the strength. **c** 53% of the strength. **d** 80% of the strength. **e** 81% of the strength. **f** 100% of the strength; 100% of the

strength (continued). **g** 80% of the strength in post-peak stage. **h** 40% of the strength in post-peak stage. **i** 0% of the strength in post-peak stage

strength and stiffness of the weak planes needs further investigation.

Funding This work was supported by National Institute for Occupational Safety and Health (NIOSH) (No. 2016-N-17733).

Data Availability Not applicable.

Compliance with Ethical Standards

Conflict of Interest The authors declare that they have no conflict of interest.

Code Availability Not applicable.

References

- Hill JL (1986) Cutter roof failure: an overview of the causes and methods for control. USBM IC 9094, Washington D.C.
- Harvey B, Robert JT, Brent E (1982) Petrology: igneous, sedimentary, and metamorphic. Freeman, San Francisco
- Esterhuizen TS, Bajpayee G S (2012) Horizontal stress related failure in bedded mine roofs - insight from field observations and numerical models, in 46th US Rock Mechanics / Geomechanics Symposium 2012, vol. 1, pp. 68–77, [Online]. Available: <https://www.onepetro.org/conference-paper/ARMA-2012-137>.
- Garg P (2018) Behaviour of laminated roof under high horizontal stress. West Virginia University
- Einstein HH, Hirschfeld RC (1973) Model studies on mechanics of jointed rock. *J Soil Mech Found Div* 99(sm3)
- Xuxu Y, Hongwen J, Kunfu F (2016) Numerical simulations of failure behavior around a circular opening in a non-persistently jointed rock mass under biaxial compression. *Int J Min Sci Technol* 26(4):729–738. <https://doi.org/10.1016/j.ijmst.2016.05.027>
- Arora S, Mishra B (2015) Investigation of the failure mode of shale rocks in biaxial and triaxial compression tests. *Int J Rock Mech Min Sci* 79:109–123. <https://doi.org/10.1016/j.ijrmms.2015.08.014>
- Wai Loong C, Asadul H, Ranjith PG, Akm S (2013) Modelling of intact and jointed mudstone samples under uniaxial and triaxial compression. *Arab J Geosci* 6(5):1639–1646. <https://doi.org/10.1007/s12517-011-0463-8>
- Hoek E, Brown ET (1980) Underground excavations in rock. Institution of Mining and Metallurgy
- Oh J, Li Y, Mitra R, Canbulat I (2017) A numerical study on dilation of a saw-toothed rock joint under direct shear. *Rock Mech Rock Eng* 50(4):913–925. <https://doi.org/10.1007/s00603-016-1142-6>
- Chiu CC, Wang TT, Weng MC, Huang TH (2013) Modeling the anisotropic behavior of jointed rock mass using a modified smooth-joint model. *Int J Rock Mech Min Sci* 62:14–22. <https://doi.org/10.1016/j.ijrmms.2013.03.011>
- Yang ZY, Chen JM, Huang TH (1998) Effect of joint sets on the strength and deformation of rock mass models. *Int J Rock Mech Min Sci* 35(1):75–84. [https://doi.org/10.1016/S1365-1609\(98\)80024-5](https://doi.org/10.1016/S1365-1609(98)80024-5)
- Lambert C, Coll C (2014) Discrete modeling of rock joints with a smooth-joint contact model. *J Rock Mech Geotech Eng* 6(1):1–12. <https://doi.org/10.1016/j.jrmge.2013.12.003>
- Chiu CC, Weng MC, Huang TH (2016) Modeling rock joint behavior using a rough-joint model. *Int J Rock Mech Min Sci* 89:14–25. <https://doi.org/10.1016/j.ijrmms.2016.08.001>
- Itasca PFC 6.00 (2018) Itasca Consulting Group Inc., Minneapolis, Minnesota, Accessed: Apr. 13, 2020. [Online]. Available: <https://www.itascacg.com/software/downloads/pfc-5-00-update>.
- Potyondy DO, Cundall PA (2004) A bonded-particle model for rock. *Int J Rock Mech Min Sci* 41:1329–1364
- Molinda G, Mark C (2010) Ground failures in coal mines with weak roof. *Electron J Geotech Eng* 15(F):1–42
- Becker JB (2013) A combined field, laboratory, and numerical study of cutter roof failure in Carroll Hollow Mine. Carroll County, Ohio
- Gao F, Stead D (2013) Discrete element modelling of cutter roof failure in coal mine roadways. *Int J Coal Geol* 116–117:158–171. <https://doi.org/10.1016/j.coal.2013.07.020>
- Murphy MM (2016) Shale failure mechanics and intervention measures in underground coal mines: results from 50 years of ground control safety research. *Rock Mech Rock Eng* 49(2):661–671. <https://doi.org/10.1007/s00603-015-0861-4>
- Ghabraie B, Ren G, Ghabraie K, Xie YM (2013) A study on truss bolt mechanism in controlling stability of underground excavation and cutter roof failure. *Geotech Geol Eng* 31(2):667–682. <https://doi.org/10.1007/s10706-013-9617-7>
- Xue Y, Mishra B (2017) Numerical simulation of size effect of laminated rock. *Procedia Eng* 191:984–991. <https://doi.org/10.1016/j.proeng.2017.05.270>

Publisher's Note Springer Nature remains neutral with regard to jurisdictional claims in published maps and institutional affiliations.